


2019

## Design and Structural Analysis of Morphing Wings

Nicholas Fernandez  
*University of Central Florida*

 Part of the [Mechanical Engineering Commons](#)  
Find similar works at: <https://stars.library.ucf.edu/etd>  
University of Central Florida Libraries <http://library.ucf.edu>

This Masters Thesis (Open Access) is brought to you for free and open access by STARS. It has been accepted for inclusion in Electronic Theses and Dissertations by an authorized administrator of STARS. For more information, please contact [STARS@ucf.edu](mailto:STARS@ucf.edu).

---

### STARS Citation

Fernandez, Nicholas, "Design and Structural Analysis of Morphing Wings" (2019). *Electronic Theses and Dissertations*. 6786.  
<https://stars.library.ucf.edu/etd/6786>

# DESIGN AND STRUCTURAL ANALYSIS OF MORPHING WINGS

by

NICHOLAS ALEXANDER FERNANDEZ

B.S. University of Central Florida, 2017

A thesis submitted in partial fulfillment of the requirements  
for the degree of Master of Science  
in the Department of Mechanical and Aerospace Engineering  
in the College of Engineering and Computer Sciences  
at the University of Central Florida  
Orlando, Florida

Fall Term  
2019

Major Professor: Samik Bhattacharya

© 2019 Nicholas Fernandez

## ABSTRACT

Many natural flyers and marine swimmers can morph their wings during a number of unsteady maneuverings. With such wing morphing they are able to control the unsteady aerodynamic forces. A number of man-made flyers, such as unmanned aerial vehicles and micro air vehicles, fly in comparable Reynolds number range, but they are yet to acquire similar morphing capabilities as natural flyers or swimmers. Moreover, the knowledge of fluid structural interaction (FSI) of such morphing wings is not well developed. Hence there is a need to investigate the FSI of morphing wings. In this thesis, a morphing wing was designed and its FSI was investigated. The wing was designed with the help of advanced 3D printing and the morphing capabilities utilized servo driven actuators. The design enabled the wing to execute spanwise bending, twisting and combined bending and twisting during a number of unsteady maneuverings. In the present work, the effect of gradual acceleration on the resultant unsteady forcing was investigated. FEA simulations were performed in order to gauge the response of the wing in different scenarios. A flat plate wing was towed in a 6-m-long towing tank and force data was collected using a 6-dof force sensor. With this method of morphing, future experiments can be performed for different unsteady cases. The analysis performed in this thesis will also be helpful in understanding more complex FSI problems applicable to morphing wings.

## ACKNOWLEDGEMENTS

I would like to acknowledge Dr. Samik Bhattacharya for assisting me in all my research and helping me achieve my goal of finishing my graduate education. The countless days spent fine tuning, designing, and performing experiments were some of my best memories despite the heat. Even when I am gone and working on my professional career, I expect to always be able to call on you for advice. I am grateful for the time I have spent Studying under you.

I would also like to acknowledge all of my fellow lab mates. Everyone helped me in many ways furthering my research as well as being there to help me enjoy sitting around waiting for simulations to finish running. I would not be where I am without them.

Finally, I would like to acknowledge my parents, Manny and Diana Fernandez. You both instilled a love for learning and a respect for higher education through your words and your actions. Your love and support is what got me through this to reach my goal. I hope to one day be able to truly show you both what your love and support mean to me. I am very proud to be your son and am honored to be a Fernandez.

## TABLE OF CONTENTS

LIST OF FIGURES	vi
LIST OF TABLES	viii
INTRODUCTION	1
Background	3
MATERIALS AND METHODS	6
Design of a Morphing Wing	6
Design of the carriage	12
Design of the Traverse in the Towing Tank	13
Details of the Towing Tank	14
Details of Force Sensor	15
Assembly and Calibration	17
Details of Analysis Procedure	18
RESULTS	26
Force Sensor Comparison	26
FEM Analysis	28
DISCUSSION	38
CONCLUSIONS AND FUTURE WORK	40
LIST OF REFERENCES	41

## LIST OF FIGURES

Figure 1: Preliminary string bending method	7
Figure 2: Preliminary model with internal channels	8
Figure 3: Bent rods and channel orientation	10
Figure 4: Measurements of bent rod in inches	11
Figure 5: Image of wing with servo attachments	11
Figure 6: Model of carriage with wing attached	13
Figure 7: Image of traverse	14
Figure 8: Rendered image of tank	15
Figure 9: Image describing force sensor dimensions and orientation	16
Figure 10: Image finalized setup	18
Figure 11: Output of CFD simulation 2b	19
Figure 12: Orientation of scenario 1	20
Figure 13: Orientation of scenario 2	21
Figure 14: Orientation of scenario 3	22
Figure 15: chart depicting Rankine velocity distribution	23
Figure 16: Example of pressure distribution for scenario 3	25
Figure 17: Graph of force data for case 1a	26
Figure 18: Graph of force data for case 1b	27
Figure 19: Graph of force data for case 1c	27
Figure 20: Visual representation of case 1a	29
Figure 21: Visual representation of case 1b	30

Figure 22: Visual representation of case 1c	31
Figure 23: Visual representation of case 2a	32
Figure 24: Visual representation of case 2b	33
Figure 25: Visual representation of case 2c	34
Figure 26: Visual representation of case 3a	35
Figure 27: Visual representation of case 3b	36
Figure 28: Visual representation of case 3c	37



## LIST OF TABLES

Table 1: Chart of material properties	10
Table 2: Specifications of force sensor	15
Table 3: Chart of pertinent information of scenario 1	20
Table 4: Chart of pertinent information of scenario 2	22
Table 5: Table of maximum applied pressures	24
Table 6: Chart of Drag Force Comparison	28
Table 7: Chart of pertinent information of scenario 1a	29
Table 8: Chart of pertinent information of scenario 1b	30
Table 9: Chart of pertinent information of scenario 1c	31
Table 10: Chart of pertinent information of scenario 2a	32
Table 11: Chart of pertinent information of scenario 2b	33
Table 12: Chart of pertinent information of scenario 2c	34
Table 13: Chart of pertinent information of scenario 3a	35
Table 14: Chart of pertinent information of scenario 3b	36
Table 15: Chart of pertinent information of scenario 3c	37

## INTRODUCTION

Natural flyers, such as birds, insects and marine swimmers such as fish, can bend or twist their wings or fins at ease. This is how they control the aerodynamic or hydrodynamic forces on their body. Engineering flight vehicles are yet to achieve the same level of dexterity. However, due to the rapid development of smart structures, we now have materials that can be morphed with the help of electrical signals or by some other means. This capability provides us with a new opportunity in wing design. In fact, few projects taken up by NASA and other leading organizations in aerospace research have looked into the feasibility of using programmable materials in wing design. However, the concept of morphing is not new. Wright Brothers used wing warping for controlling the roll of their aircraft.

Modular morphing is a concept where part of a structural member changes its shape or geometry under excitation of external control signals (Sofla et al. 2010). For example, in an aircraft, part of the trailing edge of the wing can be deformed to avoid flow separation (Lyu and Martins 2015). Such selective shape-changes or morphing is feasible now, thanks to the rapid development of smart materials (Barbarino et al. 2014). A two-decade joint project between DARPA, NASA, AFRL and industry partner FlexSYS has advanced the field towards morphing flight tests (Scherer et al. 1999). This program has now demonstrated multiple flight tests through the Adaptive Compliant Trailing Edge project (most recently this past month out of NASA Armstrong!). Despite this technological breakthrough, the effect of dynamic morphing on the unsteady flow, and the related fluid-structure-interaction (FSI) are yet to be explored

systematically, and consequently there are many unresolved issues (Valasek 2012). For example, when a gust hits an aircraft, which mode of morphing is beneficial, or how fast to morph.

In sea-based aviation such unsteady environments are more of a rule than exception (Reddy, Toffoletto, and Jones 2000). For example, when approaching a ship for landing, an aircraft faces the strong disturbances from the turbulent ship-air-wake. In such cases, it can use morphing to gain stability. However, the mode of morphing is still an unresolved question. Moreover, we are yet to fully understand how the optimum morphing parameters scale with the strength of the disturbance. Finally, what are the effects on the structural integrity of the aircraft when it is subjected to unsteady loads? The answers to these questions hold the key for designing morphing structures with better aeroelastic responses. These questions, however, cannot be answered by studies employing steady-state analysis and fixed-configuration testing (Gül\kiat 2010). To resolve these issues, this project will study the transient fluid-structure interactions of modular high-stiffness structures to find out the optimal morphing configurations. The goal of the proposed work is to study such coupled interactions during a dynamic morphing stage. Structural testing and flow field measurements will be performed to understand the transient dynamics of such coupled fluid-structure interactions. Our goal is to develop optimized modular morphing strategies. Reduced order models will be developed for the unsteady flow-field, which will be used for developing a closed-loop feedback control system. The impact of modular morphing in such unsteady environment will also be analyzed with the help of Finite Element Analysis (FEA). The outcome of this research will help in designing morphing wings with improved aero-structural tailoring which will be beneficial in the gusty environment of ship-air-wake.

## Background

The aerodynamic properties of an aircraft are largely decided by the shape of its wings, fuselage and various appendages attached to its body. Fixed-wing aircrafts, in particular, commercial airliners are mostly designed for a fixed operational envelope. However, advanced fighter jets are expected to be multi-role aircraft, capable of performing sharp maneuvers even under the most hostile conditions. For sea-based aviation, additional constraints are placed on fighter aircrafts as they are required to take-off and land within very short distances and need to have foldable wings and lower physical footprints. Moreover, during take-off and landing, the aircraft may also be subjected to severe gusty winds coming from the ship structure (Wadcock et al. 2004). Such disturbances are mostly generated by the vortices that are created in the ship air wake.

With such an increased operational envelope, it's practically impossible to design an aircraft with conventional control surfaces which can perform under varying unsteady environments. Shape morphing, on the other hand, can be beneficial in this regard [(Sanders, Eastep, and Forster 2003); (Johnston et al. 2007); (Gern, Inman, and Kapania 2005); Gern, Inman, and Kapania 2005)]. With rapid development in smart-material technology, especially, micro-fiber composites and programmable materials, it is now possible to design wing-shapes that can change its geometric shapes to adapt to its environment or to the given mission profile (Barbarino et al. 2014). Shape memory alloys (SMAs) and adaptive materials have been employed to design morphing wings for UAVs and MAVs. Application of SMAs greatly reduces the weight of the vehicle due to exclusion of conventional flaps, slats and related actuators (Barbarino et al., 2011). In addition to this, the capability of shape change can be used to selectively alter the flow over the

wing to gain performance benefits during a particular unsteady flow situation (Ghommam et al. 2012). For example, the wing can morph to change the wing twist (Pecora, Amoroso, and Lecce 2012), the planform, alter the wing sweep (Grant, Abdulrahim, and Lind 2006), or change the camber by modifying the trailing edge (Shili, Wenjie, and Shujun 2008), etc.

Much of the analysis of morphing wings has focused on developing a structure that can transform between two (or more) nominally static shapes. For example, researchers have proposed bistable composite shells that can snap between two positions (Schultz 2007). Others examined variable levels of in-plane precompression on membranes to enhance actuation capability (Vos et al. 2007). Some researchers have considered morphing that depends on other factors and so could vary regularly in time, but operation is still typically in steady state. For example, a morphing rotor can exhibit chord extension based on the rotor speed, but the rotor speed does not typically vary quickly except in discrete transitions (Johnson et al. 2008). However, none of these analyses have focused in any detail on either the fluid-structure interaction or the transient structural dynamics associated with the morphing process.

Although the development of smart structures has made morphing a realizable goal, the fluid-structure-interaction (FSI) aspect of morphing has not received adequate attention. Few questions are yet to be understood in their entirety:

1. When to morph?
2. How to morph?
3. What are the optimum morphing parameters?

These three questions are coupled and their answers are largely dependent on the unsteady environment under which morphing is warranted. The selection of optimum morphing parameters,

however, also need to take into account the structural aspect. The majority of research on morphing wing aerodynamics is modeled on the assumptions of steady inviscid flow. This is mainly due to the lack of experimental facilities, such as specialized wind or water tunnels to recreate gusty atmosphere. Because of using steady aerodynamics, the loads coming on to the structure are often miscalculated. Hence to properly calculate the net change in structural load caused by morphing in an unsteady environment, one must take into account the transient dynamics associated with morphing. This is exactly the motivation of the proposed research. Here, we would like to investigate the fluid structure interactions of different morphing configurations for gust alleviation and improved stability.

## MATERIALS AND METHODS

### Design of a Morphing Wing

The model, for this experiment, was decided on after going through many different designs and iterations. This section of the paper will discuss the process of designing a morphing wing able to meet the many criteria for the experiment.

The criteria associated with ensuring a properly functioning experiment are:

1. The design must be non-damaging so that the experiment can be run multiple times.
2. The wing must have the capacity to create a tip deflection of at least 20 degrees.
3. The wing must have the ability to withstand being towed through water at a speed of .3 m/s.
4. The wing must have the ability to bend without compromising the smoothness of the wing's outer surface.
5. The wing must be constructed in a way that allows the necessary PIV experiments to be conducted.
6. The wing must be capable of being interchanged easily.

The main challenge in coming up with designs was finding a way to create the required deflection without compromising the surface of the wing. When looking into methods of bending, many of the methods were either too costly, such as manufacturing the set up using soft robotics, or sacrificed aspects of the criteria above, such as bending the wing using strings on the outside. The conclusion was made that the method of bending needed to be from inside the wing itself,

while maintaining a thin profile. As a result, two designs were created that could meet these criteria.

The first design utilized a series of strings and 3d printed components that would be used to resemble a bone and joint structure. Between the joints, a rubber material would be used in order to make the components stay in line when no tension was applied to the string. Figure 1 is an image demonstrating this type of bending.

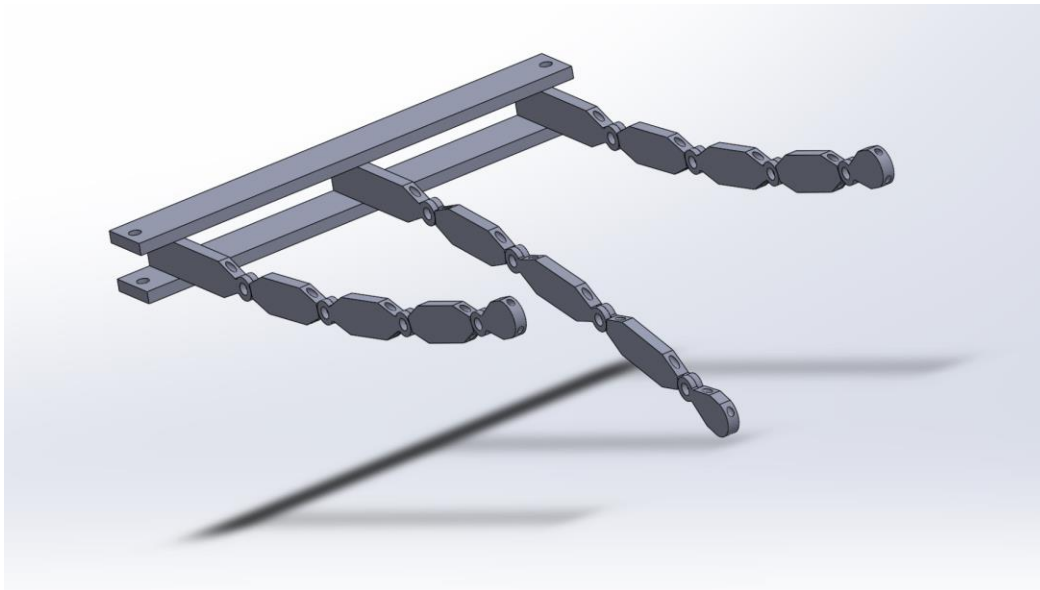


*Figure 1: Preliminary string bending method*

As the string was threaded through the channels in the components, the tip would deflect due to the applied torque. This design allowed for the wing to have many configurations depending on the number of arm segments put into the wing. This variability made each wing very adaptable so that many possible cases could be tested with each wing manufactured. A major disadvantage of this design is that the components have to be quite large for a motor to be able to create enough



torque to pull the string effectively. Another downside is the rigidity of the axis that is not rotating. When implemented, it caused irregular deformation of the wing.

For the second design method I determined that there was no need for a lot of variability in terms of bending angle. With this determination, I decided to attempt to use a fixed curved structure that would create the desired bending shape while also allowing the wing to transition smoothly between a flat and bent plate. After several iterations, a pre-bent rod was decided on allowing it to be rotated in order to make that transition. In terms of the outer part of the wing, a material that was flexible enough to meet the desired bending angle, while having enough structural integrity in order to not flop around unnecessarily, needed to be found. Many materials were considered such as nylon, different strengths of silicone rubber, and different 3d printable materials. Figure 2 is a preliminary model of this idea.



*Figure 2: Preliminary model with internal channels*

For this design, motors will attach to the rods and rotate them up to 90 degrees to get the desired bending profile. This design's main benefits are the reliability of the bend, as well the ease of rotation. Since the rods need to rotate in the gaps provided in the skin, only a low amount of torque is required to make the design work effectively. The main downside of this design is that for every different angle you want to test, a new wing and set of rods need to be manufactured. If many different angles need to be measured, the cost of materials and manufacturing escalates dramatically.

In order to meet most criteria, a design using bent rods inside of a skin was decided on. In order to reduce the cost of experimentation, the rest of the setup was designed to be able to function with different wings and rods. The design of the rest of the setup is described later in this paper.

Figure 3 shows the way the rods are bent as well as a section cut view of the wing. The channel in the middle of the wing allows the rods to rotate which then makes the wing bend in the desired fashion. The interior channels of the wing were changed from the initial model for two reasons. The first was because there was instability on the lower tips of the wing while it was flat. And second, the change in orientation allows for the rods to bend in opposite directions and create a unique profile.

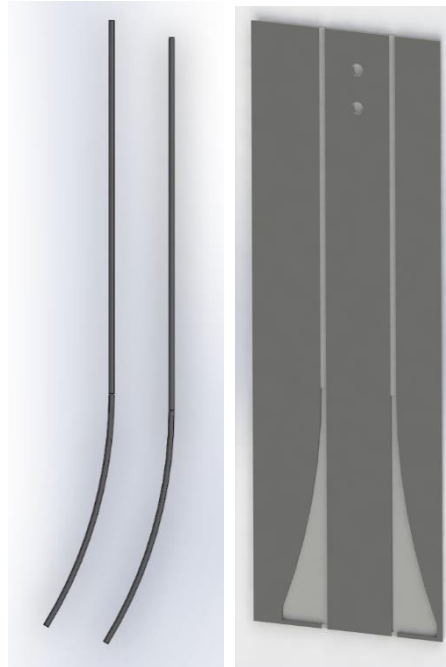


*Figure 3: Bent rods and channel orientation*

Many iterations were done in order to maximize the bending while keeping a 3:1 aspect ratio and a .7 flexion ration. These criteria were set as the goal due to many examples in nature, such as a bird or a fish having these important aspects. The final design chosen is able to meet all of the criteria. The design uses a flexible 3D printed wing and a set of bent hardened steel rods. The properties of the material and details of the bend are stated in table 1 and figure 4.

*Table 1: Chart of material properties*

Material	Aguilus 30
Density(Kg/m <sup>3</sup> )	1145
Poissons Ratio	0.47
Youngs Modulus(Mpa)	20

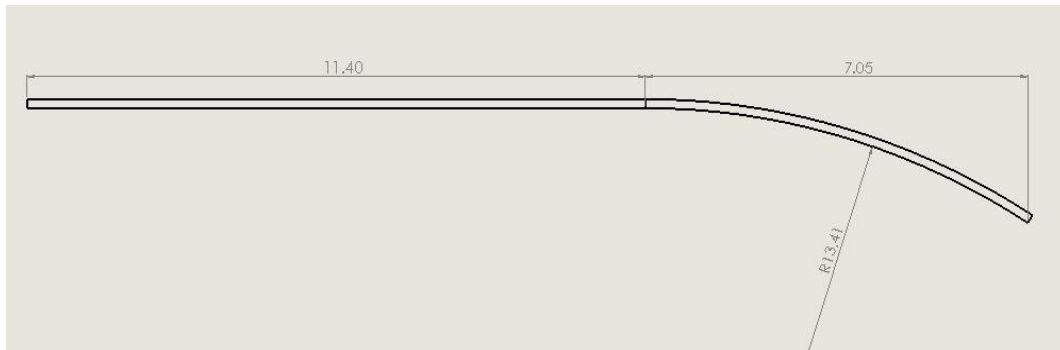


*Figure 4: Measurements of bent rod in inches*

To move the rods, 2 servo motors with custom 3d printed attachments were used. These attachments gripped the rods using a series of bolts to hold the rod in the desired position. The servo motors allowed us to control the exact speed and degree of rotation. The full system for motion is depicted in figure 5.

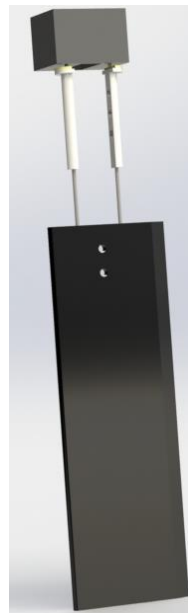


*Figure 5: Image of wing with servo attachments*

## Design of the carriage

The carriage is what connects the wing to the traverse. To be able to optimally perform the experiment, the Carriage needs to be lightweight, adjustable, and be able to attach a high spec camera to it. It is designed using 80-20 aluminum due to its ease of use and light weight. With channels built into the 80-20 material, the carriage is highly adjustable. By simply loosening a few bolts, and sliding individual beams into place, a variety of test cases, and camera orientations can be achieved simply and quickly. The camera attached to the carriage, needs to be able to view the wing as it the wing goes through the water. In order to achieve a clear camera view, a transparent acrylic sheet was used as a skim plate. The acrylic sheet was made of 2 components, a square sheet acting as a skim plate and a round dial used as a second check for guaranteeing the angle of attack. Both parts have lines etched into them in giving a close measure of the angle of attack. Figure 6 is the cad model depicting the carriage.

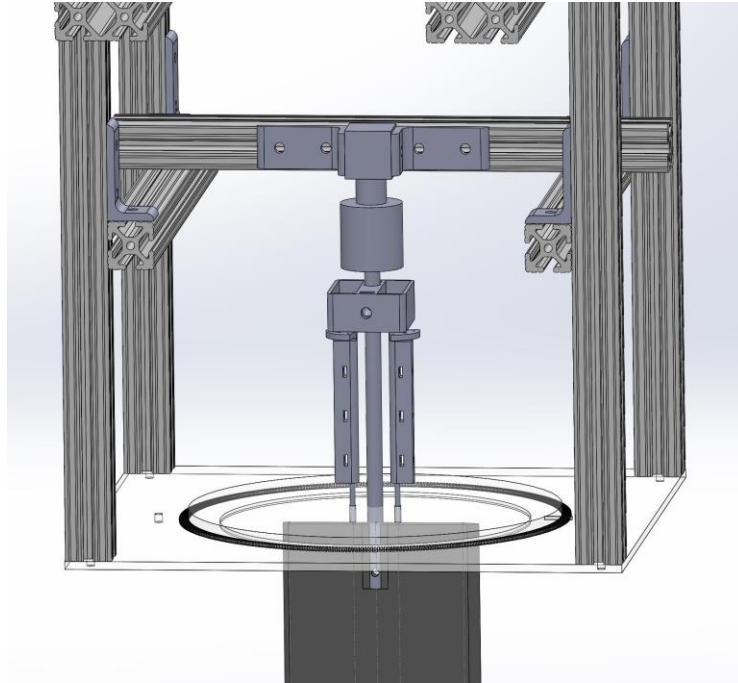


*Figure 6: Model of carriage with wing attached*

### Design of the Traverse in the Towing Tank

In order to create the scenario of the wing passing through a fluid, we attached the set up described in the previous sections to a traverse. The traverse allowed for the control of speed, acceleration, and distance of the carriage. The traverse has two tracks that are kept in sync by a torsion bar attached to both tracks.

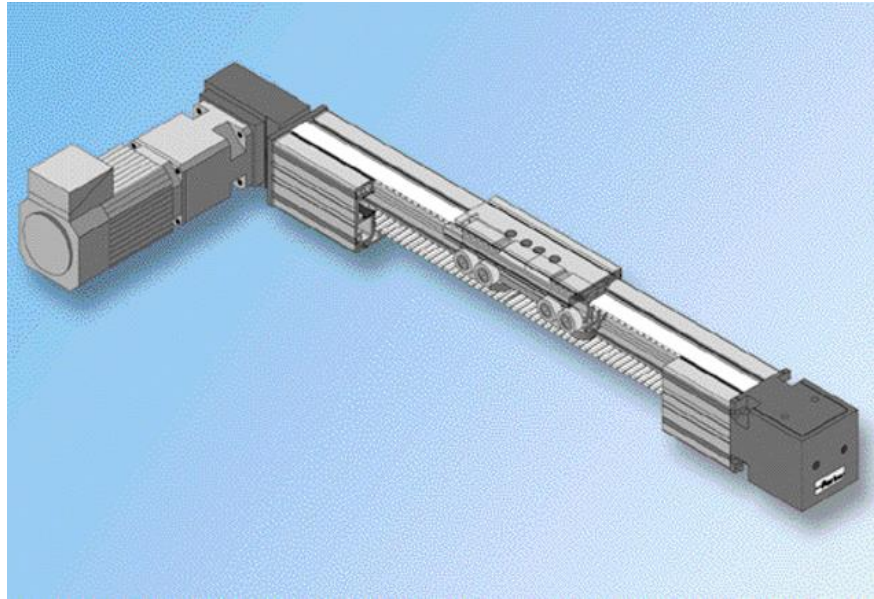


*Figure 7: Image of traverse*

### Details of the Towing Tank

The traverse is held above a large tank that holds the water for the experiment. The tank is six meters long, one meter wide, as well as one meter tall. The first and last meter of the tank has metal side panels, inner four meters contains glass side panels. The glass allows the use of lasers to go through the water for our PIV experiments. The traverse is held above the Towing tank by a structure made of 80-20 Aluminum.

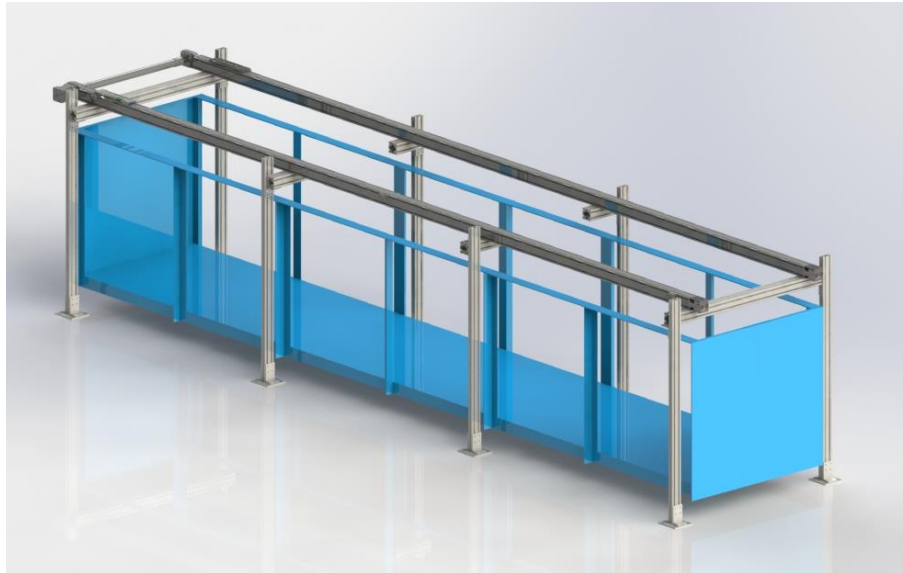


Figure 8: Rendered image of tank

### Details of Force Sensor

In order to get accurate data. A force sensor was used between the wing and where it attaches to the carriage. It was oriented to where the y axis goes along the length of the tank, the x axis is perpendicular top that, and the z axis is up and down. This setup allows us to read the forces applied to the wing during motion. The resolutions of the different axis of the force sensor are depicted in table 2.

Table 2: Specifications of force sensor

Nano25	Fx	Fy	Fz	Tx	Ty	Tz
	1.00 %	1.00 %	1.00 %	1.25 %	1.25 %	1.25 %
	Rated Fxy		Rated Fz	Rated Txy		Rated Tz
SI-125-3	125		500	3		3
	Fx Window	Fy Window	Fz Window	Tx Window	Ty Window	Tz Window
	1.250	1.250	5.000	0.038	0.038	0.038
Force Units			Torque Units			
N			N-m			



To collect data, the force sensor is connected to a DAQ which reads the output in the force sensor and translates it into usable data on the computer. The data can be erratic so some filtering was done to smooth out the data. Figure 9 is a depiction of the force sensor with dimensions.

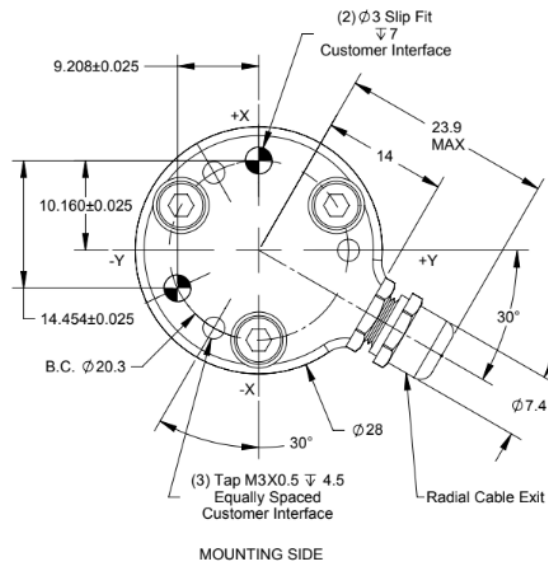
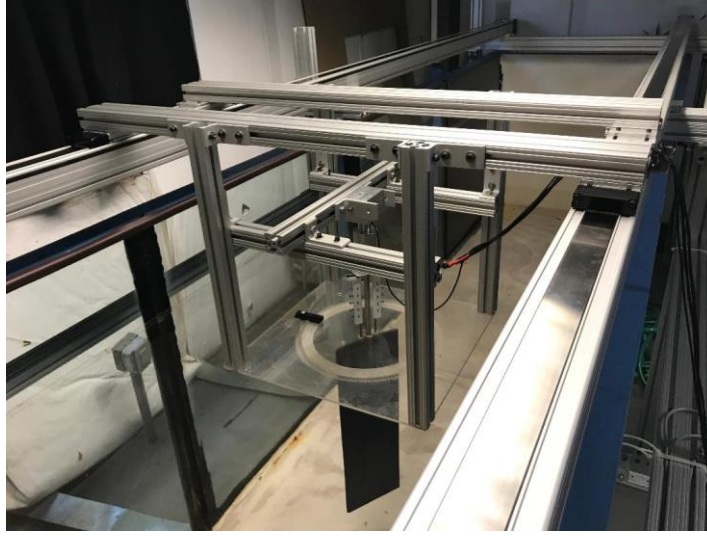


Figure 9: Image describing force sensor dimensions and orientation

To ensure quality data, the force sensor was calibrated by attaching known loads and checking the read out on the computer. As can be seen below, a force of 1000g is applied in the negative z direction of the force sensor. The computer then shows a readout of 980g.

## Assembly and Calibration

Once all the components were designed and manufactured, extensive time and effort was put into the assembly and calibration of the experiment. To start, the frame holding the traverse was leveled to within a cm using laser leveling equipment. With the base leveled, the traverse was then put on top of it and mounted in place. The traverse needed to be almost exactly parallel for it to function correctly. In order to get reliable data, both tracks were leveled to be horizontal plus or minus .05 degrees as well as making both tracks parallel to each other plus or minus .005 degrees. In order to do this more laser leveling equipment was used. As a double check and for fine adjustments, a series of measurements with a digital level was used. When leveled, a custom-made clamp was used in order to fasten the traverse to the base. After the traverse was securely in place, the carriage needed to be attached to the load attachment plate. Using custom built adapter plates, and using the digital level to ensure the carriage is held correctly, the carriage is connected and ready for the wing. After connecting the servo motors and mounting rod to the carriage, the wing and internal rods are attached from under the acrylic plate. After attachment to the carriage, the wing is then oriented to the correct angle of attack by using the correct attachments for the servo holder as well as the dial on the acrylic plate being fastened. With all this done, the camera is mounted onto the crossbar and aimed at the desired segment of the wing. The focus and aperture are then optimized for the PIV experiments required settings. These adjustments are done using a calibration plate. Once all this is wired to the DAQ along with the force sensor, the experiment is ready to start. Figure 10 is an image showing the complete set up ready for experimentation.



*Figure 10: Image finalized setup*

### Details of Analysis Procedure

Finite element analysis was performed on multiple scenarios that the wing could go through. In order to mock the scenarios, the CAD model was imported to Ansys workbench, and using a combination of forces and boundary conditions, the mock scenarios could be created. A total of three scenarios with 3 different velocities or applied forces in each scenario were performed.

In order to calculate the pressures for each scenario, the equation 1 was used.

$$P_{applied} = \frac{1}{2} \rho C_D V^2 \quad (1)$$

Where

$$\rho = 997 \frac{Kg}{m^3}, \quad v = \text{respective velocity}, \quad C_D = \text{Coefficient of Drag}$$

For all scenarios, a CFD simulation was run in order to determine the coefficient of drag. This was done by performing a steady state flow analysis of each scenario. For the mesh, I went with an oak tree type with 4.9 million cells. The mesh was more refined near the surface of the wing. For boundary conditions, there was an initial condition of pressure being at atmospheric pressure and initial velocity of zero. The inlet had a velocity boundary condition of the cases respective velocity. The outlet has a pressure outlet boundary condition. The plate has a no slip boundary condition as well. After each simulation is run, the coefficient of drag was output similar to figure 11. This data was then used for the equations above to determine the equivalent pressure to mimic these velocities.



Figure 11: Output of CFD simulation 2b

For the first scenario, a configuration of forces which mimicked a 90-degree angle of attack was used. This was done by fixing the top of the wing and applying a uniform pressure perpendicular to the flat side of the wing.

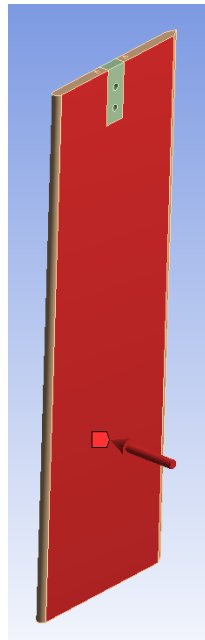


*Figure 12: Orientation of scenario 1*

For each case in this scenario, the pressure on the wing was changed to mimic different velocities. These velocities are .3 m/s, .2 m/s, and .1m/s. Table 3 shows all of the forces applied in figure 12.

*Table 3: Chart of pertinent information of scenario 1*

AOA	Velocity (in/s)	Velocity (m/s)	Cd	Applied Pressure(psi)	Applied Pressure(pa)
90 degree	3.93701	0.1	1.65	0.001192974	8.22525
	7.87402	0.2	1.588	0.004592588	31.66472
	11.81103	0.3	1.52482	0.009922202	68.4110493

For the second scenario, a configuration of forces which mimicked a 30-degree angle of attack was used. This was done by fixing the top of the wing and applying a uniform pressure at an angle of 30 degrees from the flat side of the wing.

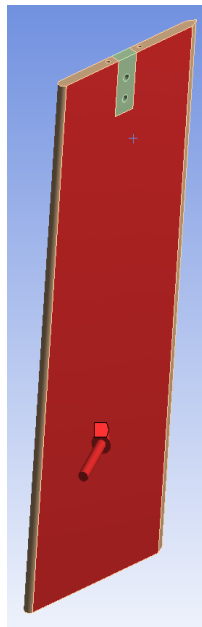


*Figure 13: Orientation of scenario 2*

For each case in this scenario, the force on the wing was changed to mimic different velocities. These velocities are .3 m/s, .2 m/s, and .1m/s. Table 4 shows all of the forces applied in figure 13. These pressures are different then the first scenario due to the difference in orientation which alters the drag coefficient of each case.

Table 4: Chart of pertinent information of scenario 2

AOA	Velocity (in/s)	Velocity (m/s)	Cd	Applied Pressure(psi)	Applied Pressure(pa)
30 degree	3.93701	0.1	0.8735	0.000631553	4.3543975
	7.87402	0.2	0.86974	0.002515341	17.34263554
	11.81103	0.3	0.90608	0.005896	40.6514138

For the third scenario, a configuration of forces which mimicked a Rankine vortex on the surface of a wing was used. This was done by fixing the top of the wing and applying pressure gradient along the chord of the wing. This gradient was applied to the flat side of the wing.

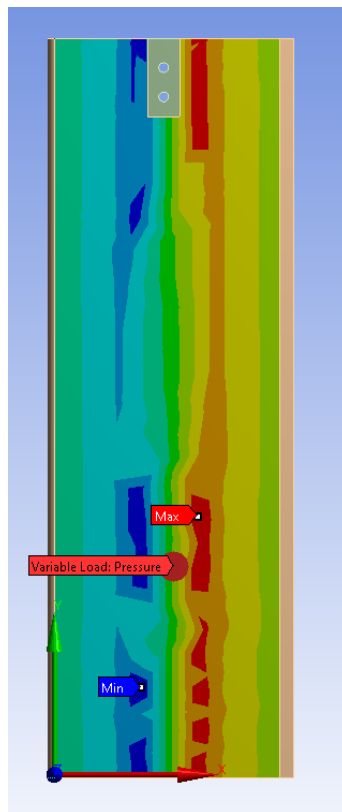
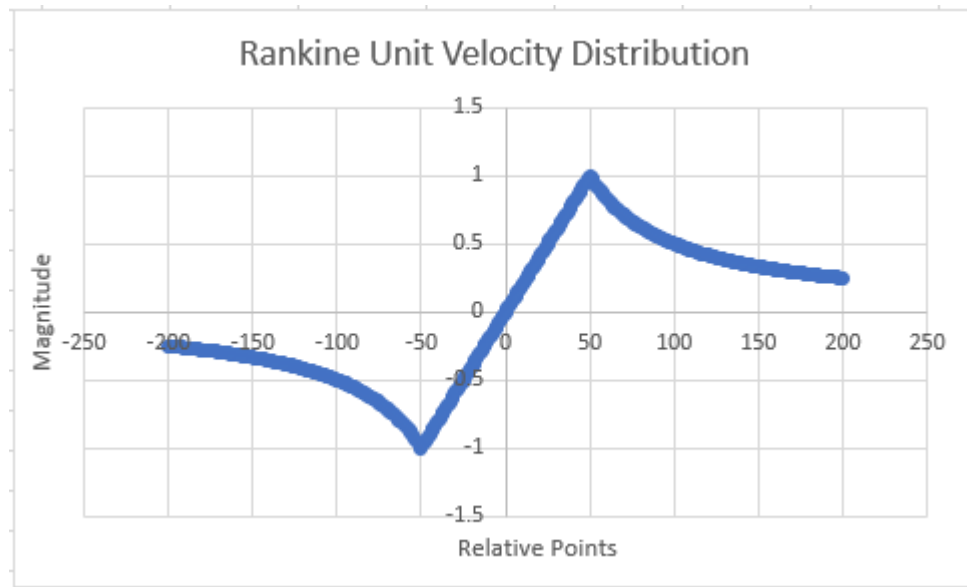


Figure 14: Orientation of scenario 3

For each case in this scenario, the pressure gradient on the wing was changed to mimic the effects of a vortex along the chord of the wing during scenario 2. The pressures mimicking these velocities were derived using equation 2 which describes the profile of a Rankine vortex. Figure 15 gives a visual representation of the equation.

$$u_{\theta}(r) = \begin{cases} \Gamma r / (2\pi R^2) & r \leq R, \\ \Gamma / (2\pi r) & r > R. \end{cases} \quad (2)$$



*Figure 15: chart depicting Rankine velocity distribution*

After creating a data set describing the Rankine vortex, the magnitude of each vortex was determined by using equation 3. This equation determines the pressure in the center of the wing with respect to the variables in scenario 2.



$$P - P_c = \rho \frac{\Omega^2}{2} (r^2 - r_c^2) \quad (3)$$

where

$$P = \text{respective pressure}, \quad \rho = 997 \frac{\text{Kg}}{\text{m}^3}, \quad \Omega = \frac{1.8v}{r_c}, \quad r = \text{chord of blade}, \quad r_c = \frac{1}{2}r$$

Using these sets of pressures, I found the difference between them and used it as the maximum magnitude of the Rankine vortex. Table 5 shows the maximum magnitude of applied pressure.

*Table 5: Table of maximum applied pressures*

Applied Pressure		
	pmax(pa)	pmax(psi)
3a	0.16915318	2.4534E-05
3b	0.67661271	9.8135E-05
3c	1.52237859	0.0002208

These magnitudes are applied to the distribution we plotted earlier and the output is a pressure distribution of the correct magnitude. Figure 16 is an example of a pressure distribution.

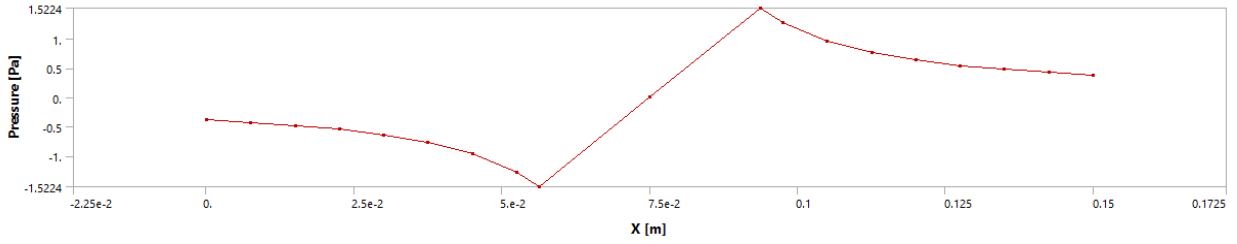


*Figure 16: Example of pressure distribution for scenario 3*

In order to ensure that the simulated data is indeed accurate, an experiment will be run following scenario 1. The force sensor data will be collected and analyzed to find the drag force applied to the wing. This data will then be compared to the drag force applied to the wing to see whether the force data is similar. To calculate the drag force for the simulations, equation 4 will be used.

$$F_d = \frac{1}{2} \rho v^2 A C_d \quad (4)$$

where

$$\rho = 997 \frac{Kg}{m^3}, \quad v = \text{respective velocity}, \quad A = .0776 m^2, \quad C_d = \text{Coefficient of Drag}$$

## RESULTS

### Force Sensor Comparison

After running the experiment, figures 17,18, and 19 were produced from the force data. With all the data points documented, the large outliers, in terms of force, were removed and the remaining data were averaged in order to find the drag force on the wing for each case.

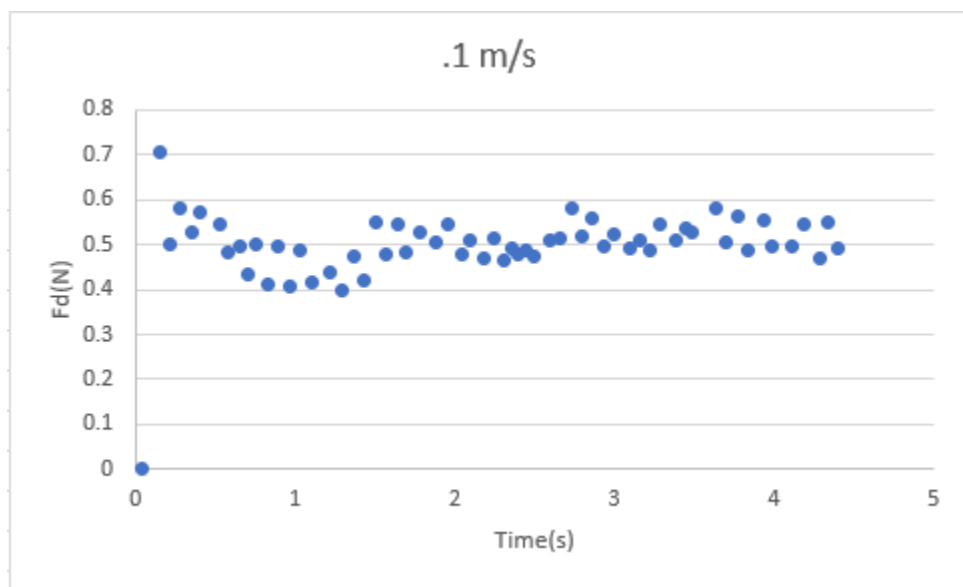


Figure 17: Graph of force data for case 1a

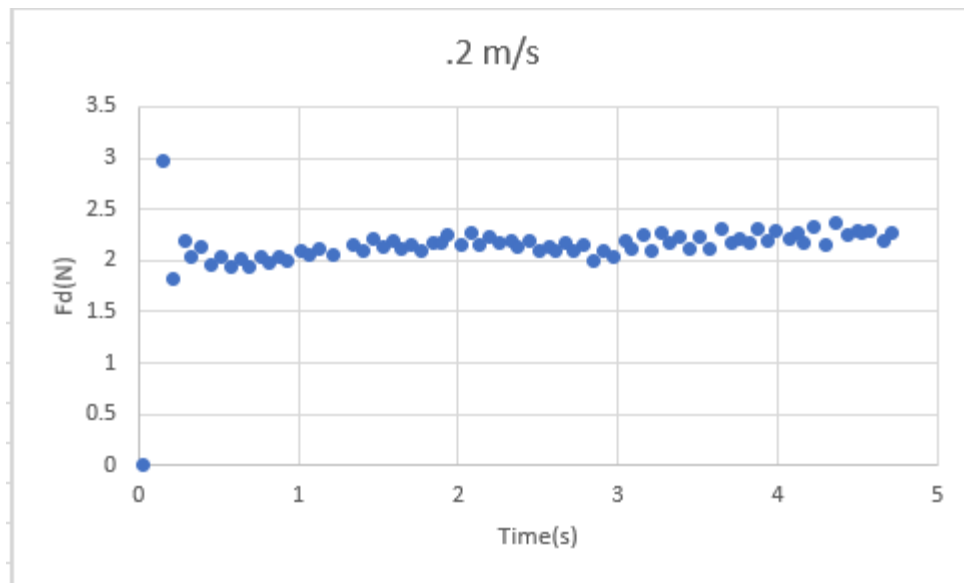


Figure 18: Graph of force data for case 1b

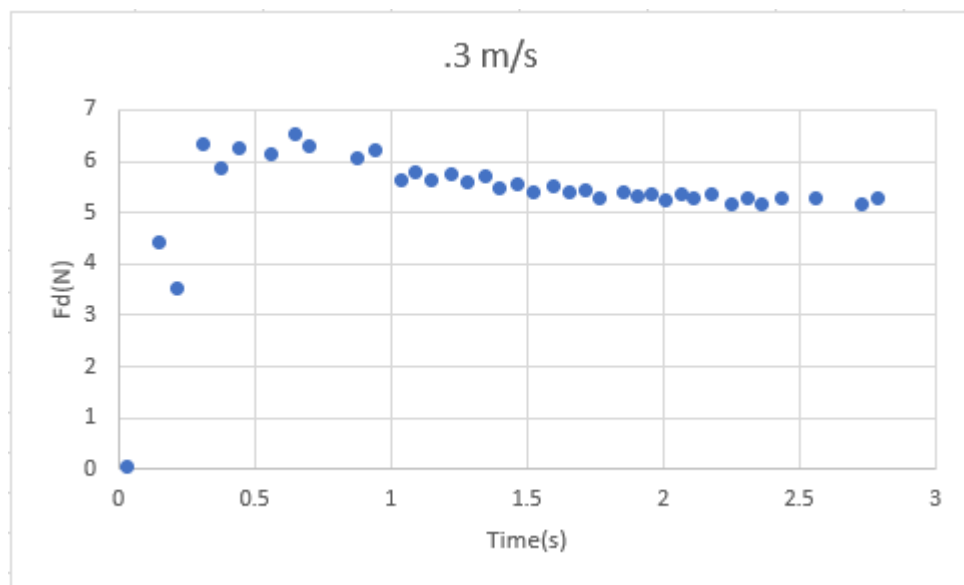


Figure 19: Graph of force data for case 1c

After calculating the average of the graphs above as well as calculating the drag force of the simulated results, table 6 was created. It has all the previous information as well as the percent error between the two results.

*Table 6: Chart of Drag Force Comparison*

Drag Force Comparison			
	Simulated	Experimental	% Error
.1 m/s	0.6391	0.5025554	27.17005926
.2 m/s	2.453	2.147074	14.2485075
.3 m/s	5.31	5.594	5.076868073

### FEM Analysis

For Finite element analysis, the main goal was to simulate the wing being towed through the water. 3 different scenarios of applied force were used on the wing in order to view the varying effects on the wing. Recorded was the displacement, stress, and strain.

For the first scenario, a uniform distributed load was applied to the surface of the wing. This orientation of force mimics a 90-degree angle of attack.

For scenario 1a, table 7 contains the output for the simulation.

Table 7: Chart of pertinent information of scenario 1a

.1 m/s			
	Deformation(m)	Stress(pa)	Strain
Maximum	0.026083	43141	0.0024362
Minimum	0	0	0

Figure 20 is a visual representation of the output property distributions on the wing.

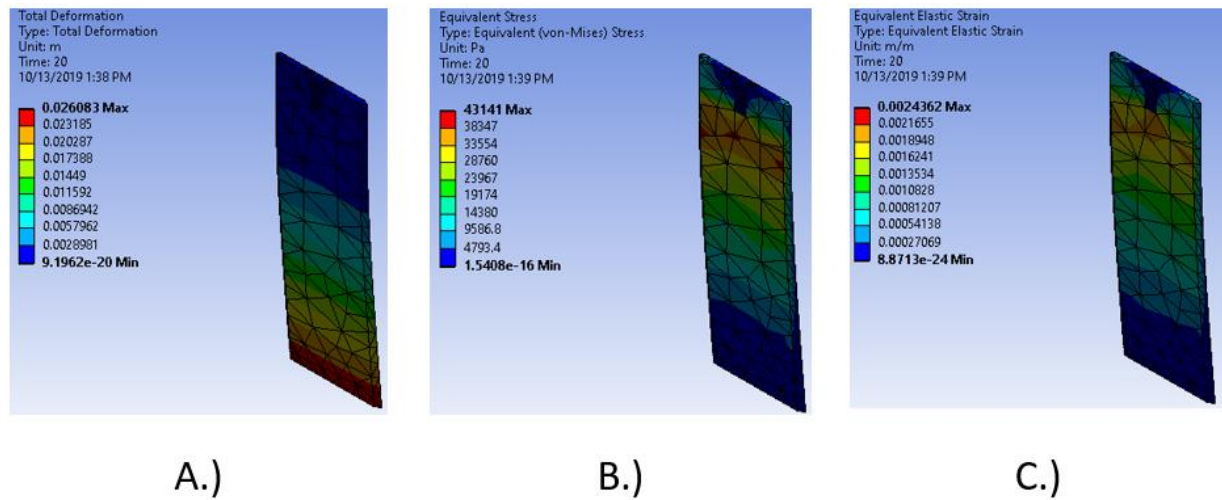


Figure 20: Visual representation of case 1a

For scenario 1b, table 8 contains the output for the simulation.

Table 8: Chart of pertinent information of scenario 1b

.2 m/s			
	Deformation(m)	Stress(pa)	Strain
Maximum	0.09513	1.58E+05	0.0089282
Minimum	0	0	0

Figure 21 is a visual representation of the output property distributions on the wing.

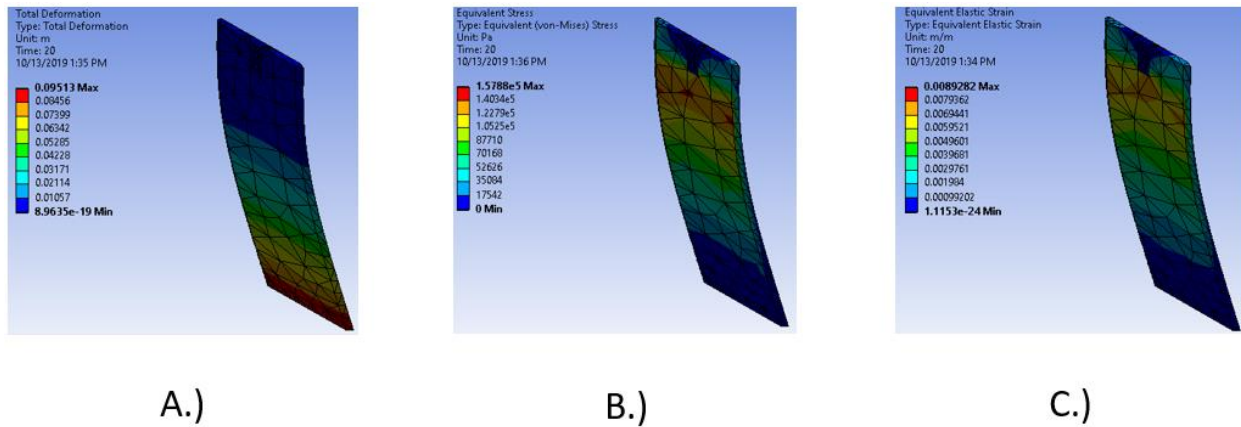


Figure 21: Visual representation of case 1b

For scenario 1c, table 9 contains the output for the simulation.

Table 9: Chart of pertinent information of scenario 1c

.3 m/s			
	Deformation(m)	Stress(pa)	Strain
Maximum	0.20553	3.41E+05	0.019289
Minimum	0	0	0

Figure 22 is a visual representation of the output property distributions on the wing.

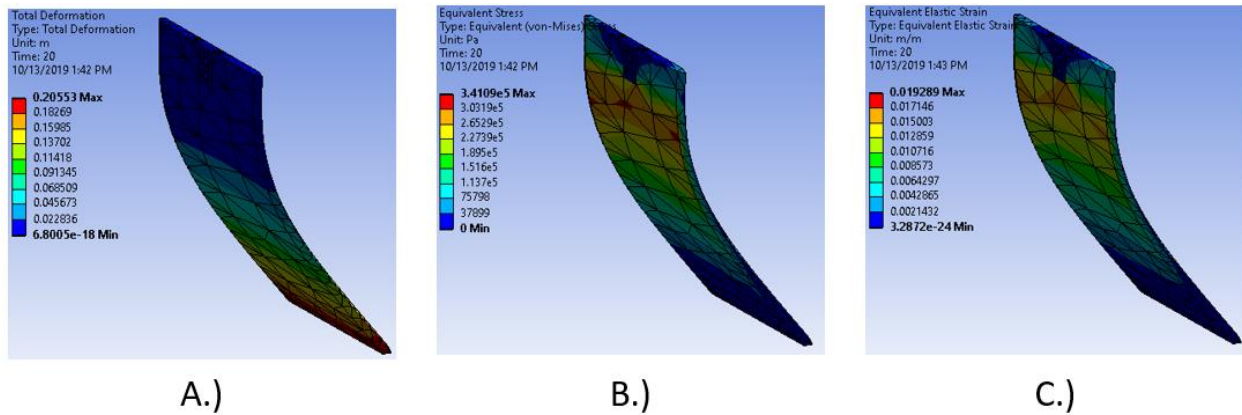


Figure 22: Visual representation of case 1c

For the second scenario, the load was applied to the wing similarly to the first scenario. The difference is that the force is set up to be an angle of attack of 30 degrees.



For scenario 2a, table 10 contains the outputs for the simulation.

Table 10: Chart of pertinent information of scenario 2a

.1 m/s			
	Deformation(m)	Stress(pa)	Strain
Maximum	0.0066108	11044	0.00064489
Minimum	0	0	0

Figure 23 is a visual representation of the output property distributions on the wing.

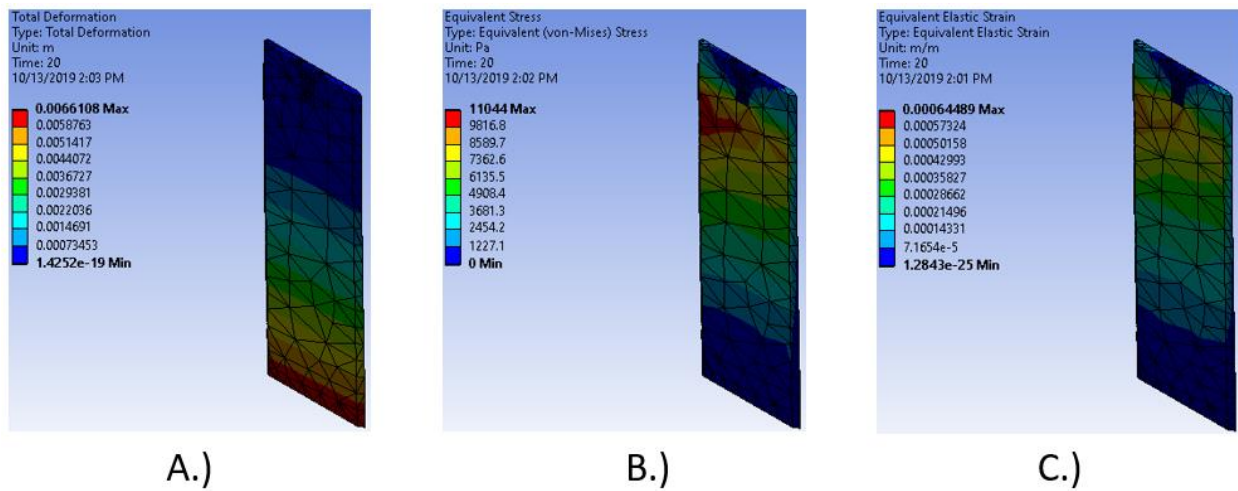


Figure 23: Visual representation of case 2a

For scenario 2b, table 11 contains the outputs for the simulation.

Table 11: Chart of pertinent information of scenario 2b

.2 m/s			
	Deformation(m)	Stress(pa)	Strain
Maximum	0.026329	43986	0.0025685
Minimum	0	0	0

Figure 24 is a visual representation of the output property distributions on the wing.

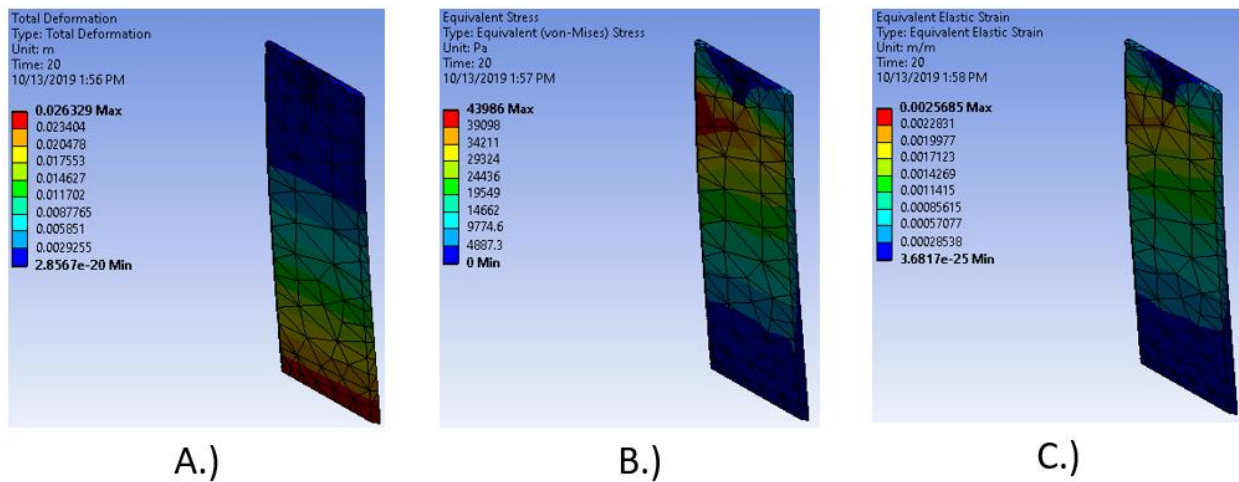


Figure 24: Visual representation of case 2b

For scenario 2c, table 12 contains the outputs for the simulation.

Table 12: Chart of pertinent information of scenario 2c

.3 m/s			
	Deformation(m)	Stress(pa)	Strain
Maximum	0.061716	1.03E+05	0.0060205
Minimum	0	0	0

Figure 25 is a visual representation of the output property distributions on the wing.

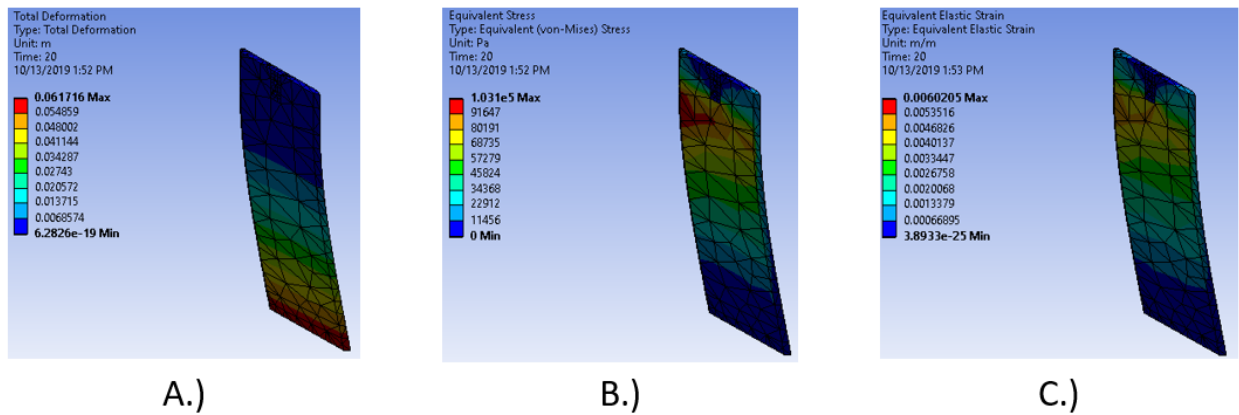


Figure 25: Visual representation of case 2c

For the third scenario, A varying load was applied along the chord of the wing mimics the pressure distribution of a Rankine vortex as it is along the wing. For the 3 scenarios, the vortices simulated will mimic the size of a vortex in situation 2.

For scenario 3a, table 13 contains the outputs for the simulation.

Table 13: Chart of pertinent information of scenario 3a

.1 m/s			
	Deformation(m)	Stress(pa)	Strain
Maximum	2.62E-05	72.474	4.29E-06
Minimum	0	0	0

Figure 26 is a visual representation of the output property distributions on the wing. Due to the small nature of the force, the scale of the visual will be increased.

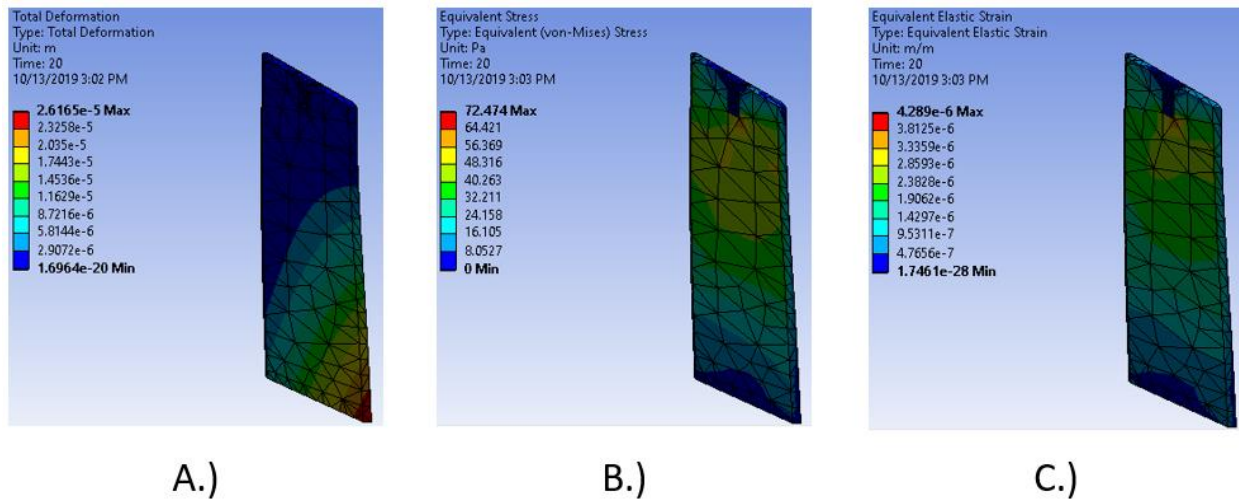


Figure 26: Visual representation of case 3a

For scenario 3b, table 14 contains the outputs for the simulation,

Table 14: Chart of pertinent information of scenario 3b

.2 m/s			
	Deformation(m)	Stress(pa)	Strain
Maximum	0.00010466	289.9	1.72E-05
Minimum	0	0	0

Figure 27 is a visual representation of the output property distributions on the wing. Due to the small nature of the force, the scale of the visual will be increased.

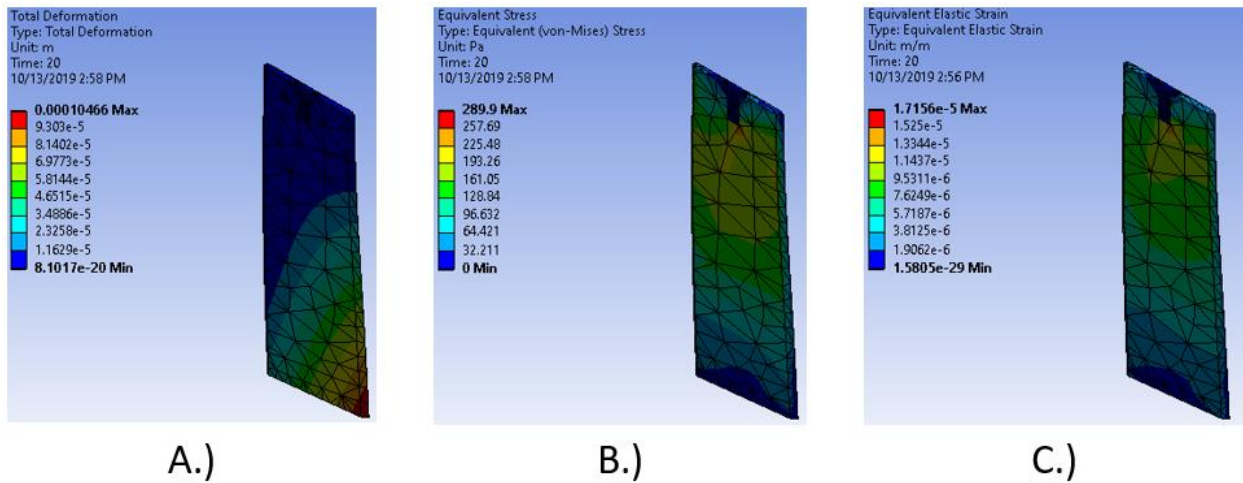


Figure 27: Visual representation of case 3b

For scenario 3c, table 15 contains the outputs for the simulation

Table 15: Chart of pertinent information of scenario 3c

.3 m/s			
	Deformation(m)	Stress(pa)	Strain
Maximum	0.00020932	6.52E+02	3.86E-05
Minimum	0	0	0

Figure 28 is a visual representation of the output property distributions on the wing. Due to the small nature of the force, the scale of the visual will be increased.

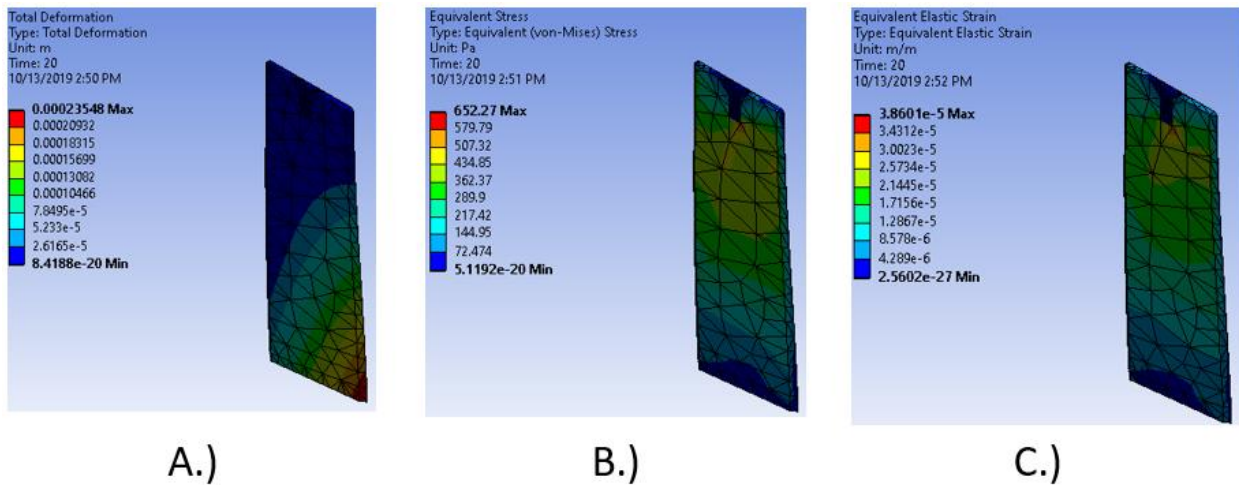


Figure 28: Visual representation of case 3c

## DISCUSSION

These simulations show that the wing is able to withstand the different velocities during towing while meeting all the other criteria described in the design of a morphing wing section of this paper.

From the drag force comparison, we can see that the simulated data has some variance from the experimental data. This can come from multiple sources of error. Case 1a had the largest percent error between the simulated and experimental data at 27.1 percent. While quite a large percent error, the scale of the force applied is actually rather small. With a small force, it is easier for percent readings to become quite large due to the sensitivity of the force sensor as well as other minor disturbances being close to scale with the applied force. I will conclude that the simulated data for this case is accurate due to this, as well as the diminishing percent error trend as the value of the forces increase in different cases. This trend is seen in the Drag force comparison chart. The percent error for the smallest force is 27 percent while the largest force is only 5 percent. In following this trend, the larger force that is applied to the wing, the more likely the experimental data and simulated data will be closer together. With this trend, and the current results for both simulation as well as experimental data, I believe that the simulation is an accurate representation of experimental results.

For Scenario 1, the expected deflection, stress, and strain was expected to be much higher than the other scenarios due to the orientation of the wing with respect to the angle of attack. The results and distributions for these properties matched the predictions made for the different properties. The deformation for all 3 cases is evenly distributed along the chord and increases

linearly along the span. The stress and strain follow a similar distribution except that both have a larger magnitude along the top part of the wing where it is fastened to the rest of the setup. This scenario created the maximum deformation as well as high stress and strain. These values are well within the margin of the wing functioning properly so therefore the wing should withstand its intended use without failure.

For scenario 2, the expected deflection was expected to be smaller than the respective velocities from scenario 1 due to the change in the angle of attack. Similar to the first scenario. The deformation seems to be evenly distributed along the chord with a little bit of an increase along the centerline. Unlike the first scenario, the stress and strain distribution are skewed to be larger along the leading edge of the wing. Although this distribution could be an issue if the magnitude of the force was larger, this distribution is within acceptable tolerances for the wing to function well while meeting the criteria for success. Similar to scenario 1, the increase in velocity seems to have an exponential growth when it comes to displacement, stress, and strain. While deformation change will decrease as the velocity increases, stress and strain may continue to exponentially increase causing the wing to fail along the leading edge.

For scenario 3, this analysis will help future researchers who are looking into the fluid dynamics of vortices along the wing. Although the effects on the wing are small in comparison to the effects from towing it through water, they can still explain discrepancies in the measured force and PIV data in future simulations.



## CONCLUSIONS AND FUTURE WORK

With the simulation and design complete, I can conclude that the wing meets all criteria to successfully perform this experiment. The wing can now be used to conduct the desired PIV experimentation and allow for a better understanding of vortices while being towed through the water.

In terms of future work, there are many routes to take. First, more detailed analysis of the wing, while it is mounted with the rest of the setup, would further the understanding of its fluid structure interaction. This will involve more complex finite element analysis and require more advanced hardware and software than currently used on this project.

This work is also helpful in the study of fluid dynamics. This data shows how a wing will deform when introduced to different scenarios that occur normally in its experimental life. This data can help future researchers understand the effects from towing the wing in different orientations. These results can also allow them to compensate when conducting experiments such as PIV.

Lastly, this work expands on one way to create the desired deformation. This design can be further optimized by changing materials or changing the orientation of components in the set up. This design might also spark another researcher to come up with a new way of morphing.

## LIST OF REFERENCES

- Barbarino, Silvestro, E I Saavedra Flores, Rafic M Ajaj, Iman Dayyani, and Michael I Friswell. 2014. "A Review on Shape Memory Alloys with Applications to Morphing Aircraft." *Smart Materials and Structures* 23 (6): 63001.
- Scherer, L. B., Martin, C. A., West, M. N., Florance, J. P., Wieseman, C. D., Burner, A. W., & Fleming, G. A. (1999, July). DARPA/ARFL/NASA Smart Wing second wind tunnel test results. In *Smart Structures and Materials 1999: Industrial and Commercial Applications of Smart Structures Technologies* (Vol. 3674, pp. 249-260). International Society for Optics and Photonics.
- Gern, Frank, Daniel J Inman, and Rakesh K Kapania. 2005. "Computation of Actuation Power Requirements for Smart Wings with Morphing Airfoils." *AIAA Journal* 43 (12): 2481–86.
- Ghommam, Mehdi, Muhammad R Hajj, Dean T Mook, Bret K Stanford, Philip S Beran, Richard D Snyder, and Layne T Watson. 2012. "Global Optimization of Actively Morphing Flapping Wings." *Journal of Fluids and Structures* 33: 210–28.
- Grant, Daniel, Mujahid Abdulrahim, and Rick Lind. 2006. "Flight Dynamics of a Morphing Aircraft Utilizing Independent Multiple-Joint Wing Sweep." In *AIAA Atmospheric Flight Mechanics Conference and Exhibit*, 6505.
- Gülkiat, Ülgen. 2010. "Fundamentals of Modern Unsteady Aerodynamics."
- Johnson Terrence, Farhan Gandhi, and Mary Frecker. 2008. "Bistable Mechanisms for Morphing Rotors." *Proc. SPIE Smart Structures / NDE 2008*. SPIE 692829.
- Johnston, Christopher O, William H Mason, Cheolheui Han, Harry H Robertshaw, and Daniel J Inman. 2007. "Actuator-Work Concepts Applied to Unconventional Aerodynamic Control Devices." *Journal of Aircraft* 44 (5): 1459–68.
- Kelley, Christopher R and Jeffrey L Kauffman. 2017. "Effect of Switch Delays in Piezoelectric-Based Semi-Active Vibration Reduction Techniques." *Journal of Intelligent Material Systems and Structures* 28 (16): 2275-2285.
- Kelley Christopher R and Jeffrey L Kauffman. 2017. "Adaptive Synchronized Switch Damping on an Inductor: A Self-Tuning Switching Law." *Smart Materials and Structures* 26 (3): 035032.

Kelley Christopher R and Jeffrey L Kauffman. 2018. "Optimal Placement and Sizing of Piezoelectric Material for Multiple-Mode Vibration Reduction." Proc. 2018 ASME Turbo Expo. GT2018-77025. June 11- 15. Oslo, Norway.

Lopp, Garrett K, Christopher R Kelley, and Jeffrey L Kauffman. 2018. "On the transient dynamics of piezoelectric-based, state-switched systems." Applied Physics Letters 112 (5): 054012.

Lopp Garrett K and Jeffrey L Kauffman. 2018. "A Synthetic Shunt for Piezoelectric-Based State Switching." Proc. SPIE Smart Structures / NDE 2018. SPIE 10595-8. March 5-8. Denver, CO.

Lyu, Zhoujie, and Joaquim R A Martins. 2015. "Aerodynamic Shape Optimization of an Adaptive Morphing Trailing-Edge Wing." Journal of Aircraft 52 (6): 1951–70.

Pecora, R, F Amoroso, and L Lecce. 2012. "Effectiveness of Wing Twist Morphing in Roll Control." Journal of Aircraft 49 (6): 1666–74.

Reddy, K R, R Toffoletto, and K R W Jones. 2000. "Numerical Simulation of Ship Airwake." Computers & Fluids 29 (4): 451–65.

Sanders, B, F E Eastep, and E Forster. 2003. "Aerodynamic and Aeroelastic Characteristics of Wings with Conformal Control Surfaces for Morphing Aircraft." Journal of Aircraft 40 (1): 94–99.

Schultz Marc R. 2007. "A Concept for Airfoil-Like Active Bistable Twisting Structures." Journal of Intelligent Material Systems and Structures 19 (2): 157-169.

Shili, Liu, Ge Wenjie, and Li Shujun. 2008. "Optimal Design of Compliant Trailing Edge for Shape Changing." Chinese Journal of Aeronautics 21 (2): 187–92.

Sofla, A Y N, S A Meguid, K T Tan, and W K Yeo. 2010. "Shape Morphing of Aircraft Wing: Status and Challenges." Materials & Design 31 (3): 1284–92.

Valasek, John. 2012. Morphing Aerospace Vehicles and Structures. Vol. 57. John Wiley & Sons.

Vos Roelof, Roeland De Breuker, Ron M Barrett, and Paolo Tiso. 2007. "Morphing Wing Flight Control Via Postbuckled Precompressed Piezoelectric Actuators." Journal of Aircraft 44 (4): 1060-1068.

Wadcock, Alan J, Gloria K Yamauchi, James T Heineck, Mark J Silva, and Kurtis R Long. 2004. "PIV Measurements of the Wake of a Tandem-Rotor Helicopter in Proximity to a Ship."

Schmid, P. J. (2010). Dynamic mode decomposition of numerical and experimental data.  
Journal